

## Metal–Organic Frameworks

Optimizing Toxic Chemical Removal through Defect-Induced UiO-66-NH<sub>2</sub> Metal–Organic Framework

Gregory W. Peterson,<sup>\*,[a]</sup> Matthew R. Destefano,<sup>[b]</sup> Sergio J. Garibay,<sup>[b]</sup> Ann Ploskonka,<sup>[c]</sup> Monica McEntee,<sup>[a]</sup> Morgan Hall,<sup>[a]</sup> Christopher J. Karwacki,<sup>[a]</sup> Joseph T. Hupp,<sup>[b]</sup> and Omar K. Farha<sup>[b]</sup>

**Abstract:** For the first time, an increasing number of defects were introduced to the metal–organic framework UiO-66-NH<sub>2</sub> in an attempt to understand the structure–activity trade-offs associated with toxic chemical removal. It was found that an optimum exists with moderate defects for toxic chemicals that react with the linker, whereas those that require hydrolysis at the secondary building unit performed better when more defects were introduced. The insights obtained through this work highlight the ability to dial-in appropriate material formulations, even within the same parent metal–organic framework, allowing for trade-offs between reaction efficiency and mass transfer.

Filtration and reaction of toxic chemicals continues to be an important research area with significant relevance to current events. The need to protect civilians, industrial workers, first responders, and military personnel is far reaching, and materials development is often highly dependent on the specific end use, whether that be broad spectrum toxic chemical removal, or highly efficient, targeted chemical removal. In all cases, significant effort goes into materials design and focuses on both the efficiency and kinetics of the chemical removal. Both of these factors are governed not only by chemistry, but also diffusion and mass-transfer considerations.<sup>[1]</sup>

Metal–organic frameworks (MOFs) have shown promise in both filtration and decontamination areas due to the ability to impart appropriate reactive functional groups while also tuning pore structure. Both reaction and diffusion rates can be optimized for the best overall removal of the toxic chemical. UiO-66-NH<sub>2</sub> in particular has been shown to be highly active

against a wide range of chemicals in both filtration,<sup>[2]</sup> as well as decontamination,<sup>[3]</sup> in addition to other areas, such as catalysis.<sup>[4]</sup>

Over the course of development, most studies have treated MOFs as pristine crystal structures. More recent efforts have focused on inducing and studying the importance of defects, such as missing linkers or nodes, on structural properties. Lillerud and co-workers has conducted systematic studies to understand the formation,<sup>[5,6]</sup> and even functionalization of defects on UiO-66-type MOFs.<sup>[7]</sup> The stability of UiO-type MOFs due to the introduction of defects has been investigated by Thornton et al.,<sup>[8]</sup> while Ghosh et al.<sup>[9]</sup> and Babarao et al.<sup>[10]</sup> have simulated equilibrium uptake of molecules, such as water and carbon dioxide. But to date, a full understanding on the importance of defects on adsorption and reactivity is lacking.

When considering the need to remove a broad range of chemical threats, however, it becomes even less understood on how to appropriately design the MOF. Enhancing diffusion by increasing defects may also reduce active sites; thus, while the removal of one chemical may be enhanced, the removal efficacy against other chemicals may be reduced. Indeed, in this research, we explored the trade-offs associated with missing linker and node defects in UiO-66-NH<sub>2</sub>. We started by synthesizing three versions of UiO-66-NH<sub>2</sub> according to established procedures (outlined in the Supporting Information) that resulted in low, medium, and highly defective structures.<sup>[11]</sup> Controlling the densities of defects was accomplished by varying both the amount of modulator (HCl) and synthesis temperature.

Figure 1 shows characterization data for the materials synthesized. Powder X-ray diffraction (PXRD) data show that the materials are consistent with one another, and correspond well to simulated theoretical PXRD patterns (Figure 1A). Peaks began to broaden as defects increased and crystallite size decreased. This is consistent with the Scherrer equation, which predicts increased broadening with smaller, and non-spherical, crystals. Thermogravimetric analysis shows the mass loss as a function of temperature (Figure 1B). Following protocols similar to those proposed by Lillerud,<sup>[5]</sup> we calculated the mass remaining for each sample, correcting for solvent and/or other adsorbed species. Calculations using Lillerud's protocol gave 0.55, 1.02, and 1.27 defects per node for the low, medium, and high-defect samples, respectively, assuming the defect is a missing linker. Attenuated total reflectance Fourier transform infrared (ATR-FTIR) data, shown in Figure 1C, are relatively con-

[a] G. W. Peterson, Dr. M. McEntee, M. Hall, Dr. C. J. Karwacki  
Edgewood Chemical Biological Center  
5183 Blackhawk Rd., Aberdeen Proving Ground, MD 21010 (USA)  
E-mail: gregory.w.peterson.civ@mail.mil

[b] M. R. Destefano, Dr. S. J. Garibay, Dr. J. T. Hupp, Dr. O. K. Farha  
Department of Chemistry and  
the International Institute for Nanotechnology  
Northwestern University, 2145 Sheridan Road, Evanston, IL 60208 (USA)

[c] A. Ploskonka  
Leidos, Inc., PO Box 68, Gunpowder, MD 21010 (USA)

Supporting information and the ORCID identification number(s) for the author(s) of this article can be found under <https://doi.org/10.1002/chem.201704525>.

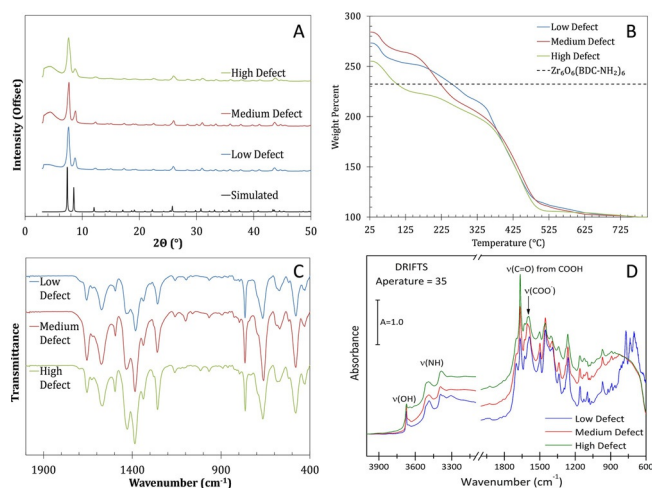


**Figure 1.** Characterization data for defective UiO-66-NH<sub>2</sub> series of MOFs. (A) Powder X-ray diffraction patterns; (B) thermogravimetric data; (C) attenuated total reflectance Fourier transform infrared transmission spectra; and (D) diffuse reflectance infrared Fourier transform absorbance spectra.

sistent for all samples, with three notable exceptions. The high-defect MOF has a peak disappear at 1098 cm<sup>-1</sup>, corresponding to the  $\delta(\text{NH}_2)$  mode. A peak at 1280 cm<sup>-1</sup> corresponding to the  $\delta(\text{OH}) + \delta(\text{CH})$  mode also begins to grow in as more defects are introduced. Diffuse reflectance infrared Fourier transform (DRIFTS), Figure 1D, was also used to better elucidate differences between the samples. There are two major takeaways from these. First, amine-stretching modes from approximately 3300 to 3500 cm<sup>-1</sup>, as well as the amine bending mode at 1500 cm<sup>-1</sup>, decrease when the sample becomes more defective.<sup>[12]</sup> These trends likely indicate that the defects are at least partially missing linkers, because less amines are present in the more defective sample(s). Second, the spectrum from the high-defect sample has a significantly higher absorbance at 1665 cm<sup>-1</sup>, which is attributed to the C=O stretching mode in the carboxylic group.<sup>[13]</sup> When defects are increased, the absorbance due to this peak increases, and the ratio of COO/C=O decreases (Figures S1 and S2 in the Supporting Information). Thus, it is apparent that some linkers in the more defective samples are not connected to the SBU. This phenomena is supported by the growth of the broad peak with increasing defects in the PXRD patterns centered at approximately 4° two theta, which Goodwin and co-workers<sup>[14]</sup> and later Lillerud and co-workers<sup>[6]</sup> attributed to nanodomains with up to one quarter of SBU clusters missing.

Nitrogen isotherms and pore-size distributions for the three MOFs are shown in Figures 2A and 2B, respectively. Data are consistent with previous studies that show increased nitrogen uptake when more defects become present in the MOF. This is likely due to the decreased density on defective samples. In the former, nitrogen uptake, surface area, and pore volume are all plotted/calculated on a mass basis; thus, a lower density material increases relative uptake. This phenomenon is reflected in the Brunauer–Emmett–Teller (BET) surface area (SA) and pore volume (PV) calculations, which range from 715 to 1154 m<sup>2</sup> g<sup>-1</sup> and 0.35 to 0.58 cc g<sup>-1</sup> for pristine-to-defective ma-

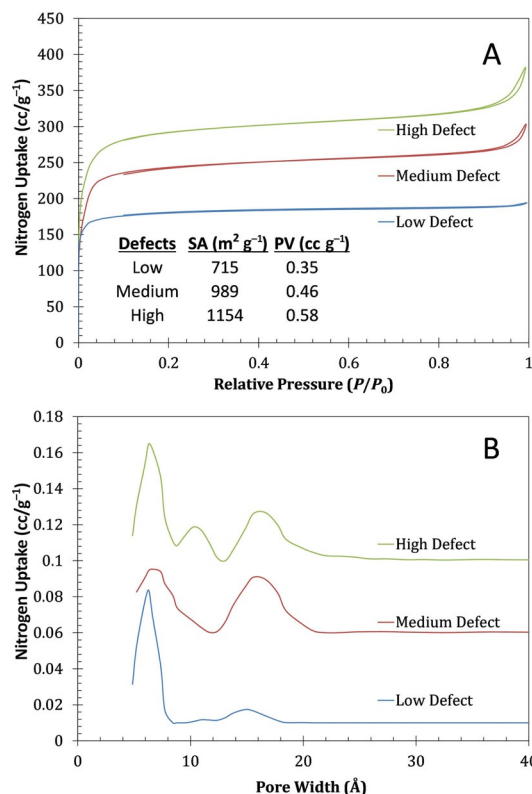


**Figure 2.** (A) Nitrogen isotherms; and (B) differential pore volume for UiO-66-NH<sub>2</sub> samples. Surface areas are reported based on BET calculation, and pore volumes are calculated at a relative pressure of 0.95.

terials, respectively. By using DFT, we were also able to obtain pore-size distributions for all three materials. As was expected, the material with the lowest number of defects had the smallest pore sizes, centered at 6 Å. The moderately defective sample showed a large decrease in pores at 6 Å, and broad increase in pores centered around 16 Å. The highly defective sample showed both, with added pores at 10 Å, representing a hierarchical microporous material.

The characterization data clearly show how physical properties are affected by inducing defects into the structure. To complement these data, we investigated the effects of defects on chemical removal properties of the same materials. Figure 3 shows microbreakthrough curves of each sample against chlorine (Cl<sub>2</sub>) gas and 2-chloroethyl ethylsulfide (2-CEES) vapor. Samples were run to saturation ( $C/C_0 = 1$ ) to obtain a mass balance and overall loading of each chemical by the three MOFs stud-

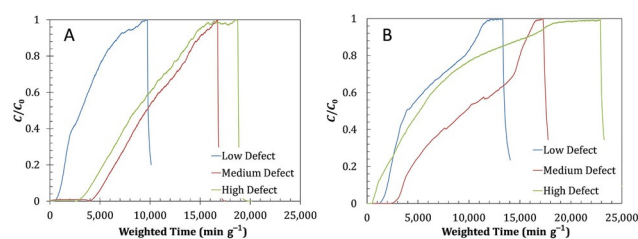


**Figure 3.** (A) Chlorine and (B) 2-chloroethyl ethylsulfide (2-CEES) microbreakthrough data.

ied; calculated values are summarized in Table 1. For both  $\text{Cl}_2$  and 2-CEES, the trends are somewhat similar. The material with the least number of defects reaches saturation first, resulting in the lowest capacity. The moderate defect sample is optimal

**Table 1.** Chemical loadings of samples.

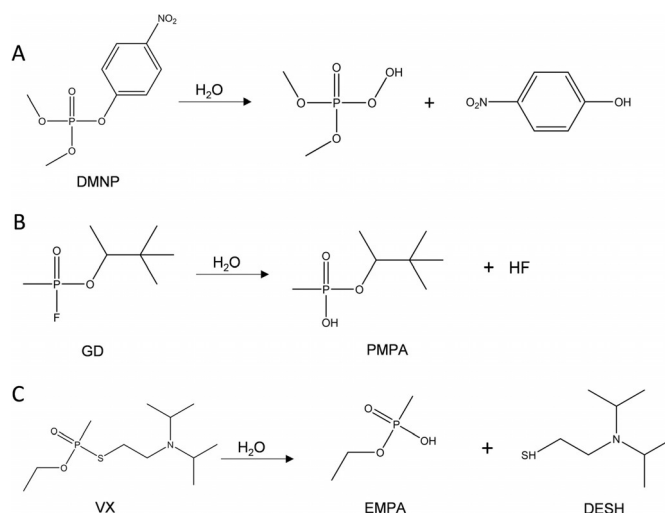
Defects	Loading [ $\text{mol kg}^{-1}$ ] <sup>[a]</sup>		$t_{1/2}$ [min]	GD	VX
	$\text{Cl}_2$	CEES	DMNP		
low	2.0	4.2	495	385	770
medium	5.6	4.4	24	25	666
high	5.1	5.1	20	19	31

[a]  $\text{Cl}_2$  and CEES loadings showed approximately 15 and 25% standard error, respectively.

for  $\text{Cl}_2$ , whereas further increasing the defects results in even higher CEES loading. This trend is interesting, considering the chemicals, but also highlights the importance of diffusion and mass transport. Chlorine is known to undergo electrophilic aromatic substitution (EAS) on  $\text{UiO-66-NH}_2$ , which occurs at the amine group of the linker. Therefore, reducing the number of linkers through the introduction of defects should reduce the overall  $\text{Cl}_2$  removal (i.e.,  $\text{Cl}_2$  adsorption). Yet the opposite is true. Instead, we see a significant increase in  $\text{Cl}_2$  removal. We propose that opening up the pore structure through defects allows  $\text{Cl}_2$  to travel further into the porous network, reacting with more linkers than in the pristine material, which likely builds up by-products on the outside of the crystal, reducing access to the active sites. This enhancement does not continue when more linkers are removed; however, indicating that a trade-off occurs between reactive sites and diffusion.

Likewise, although 2-CEES and actual mustard agent (i.e., HD, bis(2-chloroethyl) sulfide) are traditionally removed by physical adsorption on porous materials, they are also reactive by hydrolytic, oxidative, or other means. In this case, we see from the rapid drop in the effluent concentration after feed termination that the removal is at least partially reactive, and again, likely at least partially occurs at the amine group of the material (Figure S3 in the Supporting Information). If pure physical adsorption is responsible for 2-CEES removal, the chemical would continue to off-gas for an extended period of time during the purge step. The same trend is seen as with the chlorine, yet in this case, the need for the linker is less pronounced and falls more in line with surface area effects.

Dimethyl 4-nitrophenylphosphate (DMNP), *O*-pinacolyl methylphosphonofluoridate (i.e., Soman, GD), and *O*-ethyl *S*-[2-diisopropylamino)ethyl] methylphosphonothioate (VX) all undergo hydrolysis reactions on  $\text{UiO-66-NH}_2$ , and the reactions are shown in Scheme 1; conversion data for DMNP are shown in Figure S4 in the Supporting Information, and Soman and VX solid-state (SS) removal data are shown in Figure 4A and 4B, respectively. Actual SS NMR spectra are shown in Figure S4 in the Supporting Information. Both chemicals were chosen as they have been previously shown to hydrolyze at the secondary building unit (SBU), although linker functionality does affect rates.<sup>[3]</sup> DMNP removal was measured in a stirred tank



**Scheme 1.** (A) DMNP; (B) Soman; and (C) VX hydrolysis mechanisms.

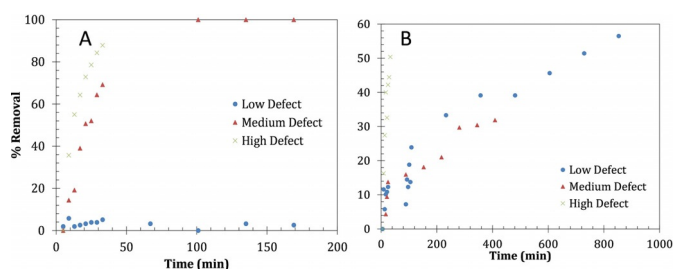


**Figure 4.** (A) Soman and (B) VX disappearance recorded by  $^{31}\text{P}$  SS NMR spectroscopy. Data measurements typically have a standard error of less than 5%.

with an *N*-ethylmorpholine buffer, with aliquots taken at discrete intervals and monitored by using a UV/Vis spectrometer for the appearance of 4-nitrophenol. The data clearly indicate enhanced reaction rates for samples with more defects, and half-life measurements shown in Table 1 correspond accordingly. The introduction of moderate number of defects to the MOF drops the reaction half-life by 20-fold, but further increases in defects have limited effect or value.

Soman removal was monitored by using  $^{31}\text{P}$  solid-state NMR spectroscopy. Equal quantifiable liquid aliquots of Soman were dropped onto each powder MOF sample, and the disappearance was monitored as a function of time. Similar to DMNP, introducing defects to  $\text{UiO-66-NH}_2$  has a profound impact on removal, with the half-life decreasing more than one order of magnitude (Table 1). This incredible enhancement shows just how important introducing even small amounts of defects have on chemical removal. Further increasing the amount of defects resulted in a further decrease of almost 40% in calculated half-life. Interestingly, this behavior is attributed partially to adsorption, and not chemical reaction, because product peaks were not seen using this technique. As was seen in the NMR spectra (Figure S5 in the Supporting Information), the by-product pinacolyl methyl phosphonic acid (PMPA) was not seen at the conditions of the experiment. The lack of PMPA could be due to a lack of spinning or reduced signal-to-noise

ratio due to adsorbed phase products. We attempted to confirm this behavior by spiking with excess water. For the low defect sample, the resulting half-life dropped two orders of magnitude to approximately 200 min, with PMPA clearly visible in the NMR spectra (Figure S6 in the Supporting Information). Yet, half-life values actually increased for defective samples (Table S2 in the Supporting Information). This is explained with water actually inhibiting the adsorption of Soman through site blocking in the defective samples, whereas excess water aids in the reactivity for the pristine, low defect MOF. We then used magic angle spinning of the high defect sample to identify the by-product. Indeed, as was shown in Figure S7 in the Supporting Information, PMPA did appear, showing that the defective materials are both highly sorptive and reactive towards Soman.

VX removal was also monitored by using  $^{31}\text{P}$  SS NMR spectroscopy using a similar procedure to Soman testing. As shown in Figure 4B, slightly different behavior was noticed for Soman. In this case, the medium defect sample exhibited similar behavior to the low-defect sample, indicating that VX is not adsorbing quickly into the pores. This is in line with the larger kinetic diameter of VX compared to Soman, and the resulting reactivity is on the surface of the MOF. Only the high-defect sample allowed VX to enter the pore, and the resulting half-life is an order of magnitude less than the other samples, because ethyl methylphosphonic acid (EMPA) is in close proximity to auto-catalyze the hydrolysis.<sup>[15]</sup>

Besides defects, one other potential factor for increased reaction rates is reduced crystal size. Indeed, the medium and high defect samples have significantly smaller crystal sizes than the low-defect sample (Figure S8 in the Supporting Information), which therefore may contribute to enhanced rates. However, when considering VX reactivity data, the medium and low-defect samples have effectively the same conversion, indicating that crystal size does not play a significant role in that reaction.

In conclusion, the introduction of defects into  $\text{UiO}-66\text{-NH}_2$  illustrates how increasing diffusion and access to pores result in higher efficacy for a variety of chemicals. Tuning the amount, and likely the type, of defect allows optimization of specific materials for specific applications. Although some chemicals may require more linkers, others require greater access to pores. Together, the optimization of activity and diffusion results in highly efficient materials.

## Acknowledgements

We thank Matthew Browe and Amedeo Napolitano for performing microbreakthrough experiments. M.L.M. thanks ORISE

for her postdoctoral fellowship. The authors thank the Defense Threat Reduction Agency for funding this research under CB3934/BA13PHM210.

## Conflict of interest

The authors declare no conflict of interest.

**Keywords:** adsorption · chemical warfare agents · defects · metal–organic frameworks · toxic chemicals

- [1] K. Vellingiri, P. Kumar, A. Deep, K. H. Kim, *Chem. Eng. J.* **2017**, *307*, 1116–1126; X. Y. Hu, S. Brandani, A. I. Benin, R. R. Willis, *Ind. Eng. Chem. Res.* **2015**, *54*, 5777–5783.
- [2] G. W. Peterson, J. B. DeCoste, F. Fatollahi-Fard, D. K. Britt, *Ind. Eng. Chem. Res.* **2014**, *53*, 701–707; J. B. DeCoste, M. A. Browe, G. W. Wagner, J. A. Rossin, G. W. Peterson, *Chem. Commun.* **2015**, *51*, 12474–12477; G. W. Peterson, J. J. Mahle, J. B. DeCoste, W. O. Gordon, J. A. Rossin, *Angew. Chem. Int. Ed.* **2016**, Ahead of Print; J. B. DeCoste, G. W. Peterson, *Chem. Rev.* **2014**, *114*, 5695–5727.
- [3] G. W. Peterson, S.-Y. Moon, G. W. Wagner, M. G. Hall, J. B. DeCoste, J. T. Hupp, O. K. Farha, *Inorg. Chem.* **2015**, *54*, 9684–9686.
- [4] A. Corma, H. Garcia, F. X. L. Llabres i Xamena, *Chem. Rev.* **2010**, *110*, 4606–4655.
- [5] G. C. Shearer, S. Chavan, J. Ethiraj, J. G. Vitillo, S. Svelle, U. Olsbye, C. Lamberti, S. Bordiga, K. P. Lillerud, *Chem. Mater.* **2014**, *26*, 4068–4071.
- [6] G. C. Shearer, S. Chavan, S. Bordiga, S. Svelle, U. Olsbye, K. P. Lillerud, *Chem. Mater.* **2016**, *28*, 3749–3761.
- [7] G. C. Shearer, J. G. Vitillo, S. Bordiga, S. Svelle, U. Olsbye, K. P. Lillerud, *Chem. Mater.* **2016**, *28*, 7190–7193.
- [8] A. W. Thornton, R. Babarao, A. Jain, F. Trousselet, F. X. Coudert, *Dalton Trans.* **2016**, *45*, 4352–4359.
- [9] P. Ghosh, Y. J. Colon, R. Q. Snurr, *Chem. Commun.* **2014**, *50*, 11329–11331.
- [10] W. Liang, C. J. Coghlan, F. Ragon, M. Rubio-Martinez, D. M. D'Alessandro, R. Babarao, *Dalton Trans.* **2016**, *45*, 4496–4500.
- [11] M. J. Katz, Z. J. Brown, Y. J. Colon, P. W. Siu, K. A. Scheidt, R. Q. Snurr, J. T. Hupp, O. K. Farha, *Chem. Commun.* **2013**, *49*, 9449–9451; M. R. DeStefano, T. Islamoglu, S. J. Garibay, J. T. Hupp, O. K. Farha, *Chem. Mater.* **2017**, *29*, 1357–1361.
- [12] L. J. Shen, S. J. Liang, W. M. Wu, R. W. Liang, L. Wu, *Dalton Trans.* **2013**, *42*, 13649–13657.
- [13] M. Karabacak, M. Cinar, Z. Unal, M. Kurt, *J. Mol. Struct.* **2010**, *982*, 22–27.
- [14] M. J. Cliffe, W. Wan, X. D. Zou, P. A. Chater, A. K. Kleppe, M. G. Tucker, H. Wilhelm, N. P. Funnell, F. X. Coudert, A. L. Goodwin, *Nat. Commun.* **2014**, *5*, 4176.
- [15] T. J. Bandoz, M. Laskoski, J. Mahle, G. Mogilevsky, G. W. Peterson, J. A. Rossin, G. W. Wagner, *J. Phys. Chem. C* **2012**, *116*, 11606–11614.

Manuscript received: September 25, 2017

Accepted manuscript online: September 26, 2017

Version of record online: October 24, 2017